

# MRIR: Integrating Multimodal Insights for Diffusion-based Realistic Image Restoration

Yuhong Zhang, Hengsheng Zhang, Xinning Chai, Rong Xie, *Member, IEEE*, Li Song, *Senior Member, IEEE*, Wenjun Zhang, *Fellow Member, IEEE*

**Abstract**—Realistic image restoration is a crucial task in computer vision, and the use of diffusion-based models for image restoration has garnered significant attention due to their ability to produce realistic results. However, the quality of the generated images is still a significant challenge due to the severity of image degradation and the uncontrollability of the diffusion model. In this work, we delve into the potential of utilizing pre-trained stable diffusion for image restoration and propose MRIR, a diffusion-based restoration method with multimodal insights. Specifically, we explore the problem from two perspectives: textual level and visual level. For the textual level, we harness the power of the pre-trained multimodal large language model to infer meaningful semantic information from low-quality images. Furthermore, we employ the CLIP image encoder with a designed Refine Layer to capture image details as a supplement. For the visual level, we mainly focus on the pixel level control. Thus, we utilize a Pixel-level Processor and ControlNet to control spatial structures. Finally, we integrate the aforementioned control information into the denoising U-Net using multi-level attention mechanisms and realize controllable image restoration with multimodal insights. The qualitative and quantitative results demonstrate our method’s superiority over other state-of-the-art methods on both synthetic and real-world datasets.

**Index Terms**—Image restoration, diffusion models, blind super-resolution, MLLM.

## I. INTRODUCTION

**I**MAGE restoration (IR) has always been a classic problem in digital image processing, aiming to convert low-quality (LQ) images into high-quality (HQ) and clear images. Typical image restoration tasks include super-resolution (SR) [1]–[3], deblurring [4]–[6], denoising [7], [8], color enhancement [9], [10], inpainting [11]–[13], compression artifact removal [14], [15], etc. Early research often focused on studying image restoration problems under the assumption of a known linear degradation type present in the image. However, real-world low-quality images often contain complex and diverse degradation types, making these methods less effective in practical applications. Therefore, BSRGAN [16] and Real-ESRGAN [17] proposed new degradation synthesis methods to model the degradation process and achieve realistic image

restoration (real-IR). As image restoration techniques have advanced, there is a significant increase in the expectation of the perceptual quality of restored images. The over-smoothed results produced by the methods mentioned above fail to meet these expectations. To address this, generative adversarial networks (GANs) have been employed to solve the real-IR problem [18]–[21]. By using adversarial loss, supervised image restoration models generate perceptually realistic details. However, GAN-based real-IR methods often introduce unnatural visual artifacts [20], [21].

Recently, denoising diffusion probabilistic models (DDPMs) [22] have achieved significant success in the field of image generation, surpassing traditional generative adversarial networks (GANs) in various downstream tasks [23]. As a result, researchers have started exploring the use of DDPMs for image restoration, incorporating high-quality generative priors from diffusion models into image restoration tasks to generate more realistic images [24]–[27]. Alongside the success of large-scale pre-trained text-to-image (T2I) models, like Stable Diffusion (SD) trained on datasets containing over 5 billion image-text pairs, which provide rich natural image priors, serving as a vast library of textures and structures, some methods [28]–[32] have attempted blind image super-resolution using pre-trained T2I diffusion models. However, these methods have not fully exploited the potential of T2I models, particularly in obtaining high-quality textual prompts from low-quality images. Furthermore, with the development of multi-modal techniques, large language models (LLMs) or multimodal large language models (MLLMs) have played a significant role in multi-modal high-quality image generation and editing tasks [33]–[36]. However, applying LLMs or MLLMs to image restoration tasks is still limited [34], [37].

In this paper, we delve into the exploration of harnessing the generative potential of pre-trained T2I models for achieving realistic image restoration. We approach the problem from both textual level and visual level perspectives, proposing a multimodal-perception realistic image restoration model (MRIR). For the textual level, to obtain high-quality textual representations from LQ images, we introduce a multimodal large language model to predict the semantic prompt of restored images from LQ inputs. Additionally, to ensure fidelity to the original image during the restoration process, we design an image embedding branch that collaborates with the text predicted by MLLM, achieving a balance between fidelity and realism. Regarding the visual level, we focus on pixel control and employ a Pixel-level Processor to extract clear features from the degraded image to control the restoration process.

Yuhong Zhang, Hengsheng Zhang, Xinning Chai, Rong Xie and Wenjun Zhang are with Institute of Image Communication and Network Engineering, Shanghai Jiao Tong University, China (e-mail: rainbowow@sjtu.edu.cn; hs\_zhang@sjtu.edu.cn; chaixinning@sjtu.edu.cn; xierong@sjtu.edu.cn; zhangwenjun@sjtu.edu.cn).

Li Song is with Institute of Image Communication and Network Engineering, Shanghai Jiao Tong University and the MoE Key Lab of Artificial Intelligence, AI Institute, Shanghai Jiao Tong University, China (email: song\_li@sjtu.edu.cn).

Finally, we employ attention mechanisms to integrate pixel control, text embedding, and image embedding to the denoising U-Net of the diffusion model. All modules collaborate to generate structurally accurate and detail-rich restored images.

Our contributions can be summarized as follows:

- We propose a diffusion-based realistic image restoration model that incorporates dual-perception of textual and visual level information.
- We utilize MLLM and refine layers to obtain effective textual control. We employ a Pixel-level Processor and multi-layer supervision to get clear pixel control.
- We integrate the control information with the diffusion model using multi-layer attention mechanisms. Our model demonstrates advanced performance on multiple datasets, as measured by various image quality metrics.

## II. RELATED WORK

### A. Realistic Image Restoration

The goal of realistic image restoration is to transform the LQ images with degradation artifacts to HQ and photo-realistic ones. Early research focused on image restoration of single degradation types, such as super-resolution [1]–[3], [38]–[40], denoising [7], [8], [41], deblurring [4]–[6], and color enhancement [9], [10]. Some researchers are dedicated to studying baseline models for image restoration to handle various types of degradation [42]–[44], but training on specific datasets is required for each degradation type. Overall, these methods often rely on specific degradation types, while real-world degradation types are typically complex and diverse, making it challenging to apply these methods in practical scenarios. Therefore, some methods [16], [17], [45] have made progress in the field of realistic image restoration by modeling the degradation process of images to simulate real-world image degradation. With the development of Generative Adversarial Networks, some studies [16]–[21] have utilized pre-trained GANs to improve the super-resolution process, reducing the smoothness of generated images and enhancing the richness of texture details. Specifically, BSRGAN [16] utilizes a randomly selected degradation strategy to enhance the richness of degradation, while Real-ESRGAN [17] employs a high-order degradation modeling process. DASR [18] proposes an adaptive super-resolution network that estimates the degradation for each input image. FeMaSR [19] utilizes a pre-trained VQGAN network for feature matching between low-resolution features and the distortion-free high-resolution prior, resulting in more realistic and less artifact-prone image generation. However, GAN-based real-IR methods often introduce unnatural visual artifacts [20], [21]. Therefore, in recent research, there is increasing interest in utilizing more advanced pre-trained generative models, such as denoising diffusion models [22], [23], [46], for image restoration to generate more realistic images.

### B. Diffusion-Based Image Restoration

With the development of diffusion models, several attempts [24]–[26] have been made to utilize DDPM [22] for addressing

image super-resolution problems. However, these methods often rely on simple downsampling linear degradation, making it challenging to apply them effectively in practical restoration scenarios. The assumption of known linear image degradation limits their practical application in complex scenes. Concurrently, other studies [28]–[32], have employed powerful pre-trained T2I models, such as stable diffusion [47], to tackle real-world image restoration problems. Trained on billions of image-text pairs, these models possess rich image priors that are crucial for real-world image restoration. StableSR [28] finetunes the SD model by training a time-aware encoder and an additional CFW module [48] to balance fidelity and perceptual quality, enabling blind image restoration. DiffBIR [29] employs a two-stage strategy to address real-IR problems. It first reconstructs an image as an initial estimate and then employs SD priors to enhance image details. The aforementioned methods rely solely on images as conditions to activate the generation capability of T2I models. In contrast, PASD [30] takes it a step further by utilizing high-level models, but the acquisition of high-level information relies on low-quality images, leading to a substantial amount of inaccurate information. SeeSR [31] trains a dedicated RAM model [49] for assistance in restoration, while CoSeR [32] trains a dedicated cognitive encoder for object categorization. However, both methods require separate training, and their restoration performance is dependent on the additional trained RAM and cognitive encoder. What's more, they perform better when dealing with images containing explicitly categorized objects, but struggle with images lacking clear category information. Therefore, further exploration is needed on how to introduce high-quality information from low-quality images to more effectively leverage the potential of pre-trained T2I models for assisting real-IR.

### C. MLLM Assisted Image Restoration

With the rapid development of text-to-image techniques, multimodal image generation has attracted increasing attention. LLMs and MLLMs have provided a range of solutions for high-quality multimodal image generation and editing tasks [33]–[36]. However, only a few works [34], [37], [50] have extended LLMs or MLLMs to image restoration tasks. Clarity ChatGPT [37] combines ChatGPT with various pre-trained image restoration models, utilizing the rich prior reasoning capabilities of LLMs/MLLMs to determine, select, and invoke appropriate image restoration base models. LLMRA [34] utilizes pre-trained MLLMs to generate descriptive textual descriptions of the input degraded images, encompassing detailed textual descriptions of low-level features in the degraded images. These descriptions are encoded as text features and serve as guiding conditions that are input into a transformer network responsible for image restoration. [50] employs MLLMs to simultaneously take input images and chat-style user requests, generating language dialogue responses and an implicit guiding prompt, which are input into the cross-attention module of the generation network through a mapping network to guide image inpainting. However, these methods are only simple applications of MLLM and are not combined with the

diffusion model to handle more realistic image restoration. SUPIR [51] applies text guidance from MLLMs in diffusion models. It's the first attempt to combine the MLLM and diffusion to realize image restoration, but the method applies the MLLM to describe the images based on the pre-restored images and does not fully exploit the inferential capabilities of MLLMs for predicting the content of the restored images.

### III. METHOD

#### A. Motivation and Overview

**Motivation.** Motivated by the remarkable success of ControlNet [52] in controllable image generation, researchers have turned their attention to employing the ControlNet architecture with the pre-trained T2I models for realistic image restoration. Thus, the quality of the generated images by the diffusion model is heavily influenced by two crucial factors: prompts and control conditions of ControlNet. Consequently, extensive research has been conducted from these two perspectives.

In terms of the textual control conditions, various approaches have been investigated. We conduct a preliminary experiment with different textual prompts. We use the PASD [30] as a baseline and employ null prompts, LQ prompts (captions generated from LQ images), and GT prompts (captions generated from GT images) to guide image restoration individually. Fig 1 illustrates the impact of different textual information on the restoration results. As shown in Fig 1, compared with generation with null prompts, incorporating textual prompts proves beneficial for generating detailed image content, and the richness of generated details increases with more detailed textual descriptions. However, due to the degradation in the LQ images, directly utilizing the captions derived from these images may lead to semantic errors. As depicted in Fig 1 (b), the prompt extracted from the LQ image results in an incorrect description, leading the T2I model to erroneously generate a plane. In fact, obtaining GT prompts for realistic image restoration is not feasible. Consequently, we aim to infer accurate and detailed textual descriptions from LQ images to guide the restoration process. Leveraging the remarkable success of MLLMs, we employ the MLLM to predict the semantic content. Taking the LQ image in Fig 1 as an example, the prompt predicted by the MLLM is as follows: "A field of ripe wheat stands against a clear blue sky, creating a picturesque sight. The golden wheat glows under the sunlight, while the serene blue sky provides a beautiful backdrop." The predicted prompt possesses accurate semantics and rich descriptive details. When used to guide the PASD restoration, it achieves comparable or even superior restoration result to the result obtained using the GT prompt, as shown in Fig 1 (d).

In terms of pixel-level control, we aim to extract clear features from LQ images to exert control over the generated image. Therefore, we employ preprocessing techniques to obtain clear features and utilize ControlNet to regulate the diffusion process.

In summary, we construct our image restoration model by considering the two aforementioned perspectives. Firstly, in the context of textual control conditions, our objective is to

infer semantically accurate and detailed textual descriptions from low-quality images, facilitating precise control over the image generation process. Secondly, for the pixel control, we aim to exploit the latent clear features from the low-quality images to effectively guide the restoration process.

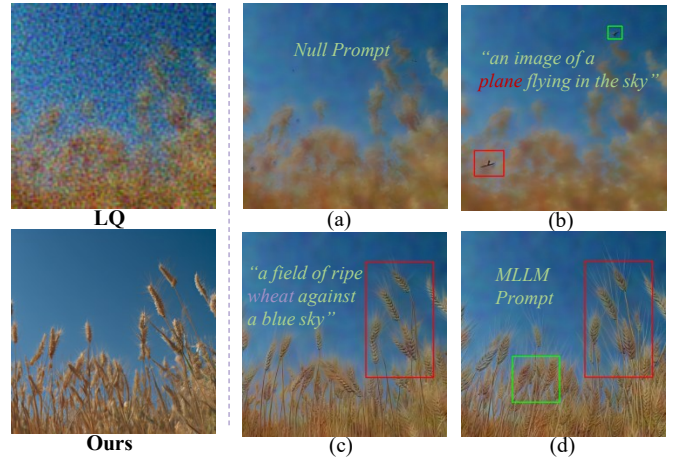


Fig. 1. The comparison of different prompts and their corresponding restoration results with PASD [30].(a)-(d) show the null prompt, BLIP prompt from LQ image, BLIP prompt from GT image and MLLM prompt predicted from LQ image and its corresponding restoration result.

**Overview.** Based on the aforementioned observations, we propose a multimodal-perception approach for realistic image restoration. To fully leverage the generative priors of pre-trained T2I models such as stable diffusion, we utilize textual level and visual/pixel level information to guide the diffusion process in image restoration, aiming to generate realistic restoration results with coherent structures and clear details. The overall framework of our model is depicted in Fig 2. We employ stable diffusion as the backbone and control the diffusion process from both the textual level and pixel level. The **textual level** includes two branches: one branch utilizes the inference capability of a pre-trained multimodal language model to predict potential restoration results from the LQ images, generating restored text embeddings. Additionally, to ensure the semantic fidelity of the generated predictions to the original LQ images, we design an image embedding branch. An image encoder extracts image embedding, and a Refine Layer is employed to correct the image embedding and mitigate the influence of degraded information in LQ images. The text embedding and image embedding collaborate as the textual level information to control the restoration process of the diffusion model. The **pixel level** control consists of a Pixel-level Processor and a ControlNet module. The Pixel-level Processor extracts potential clear features from the low-quality image, while the ControlNet module utilizes these features to generate pixel control in the latent domain, thus enabling spatial structural control in the diffusion process. Finally, the denoising U-Net utilizes text embedding, image embedding, and pixel control to generate high-quality restoration results. Our model is trained end-to-end without requiring any additional training while SeeSR and CoSeR need additional training to obtain the semantic information from

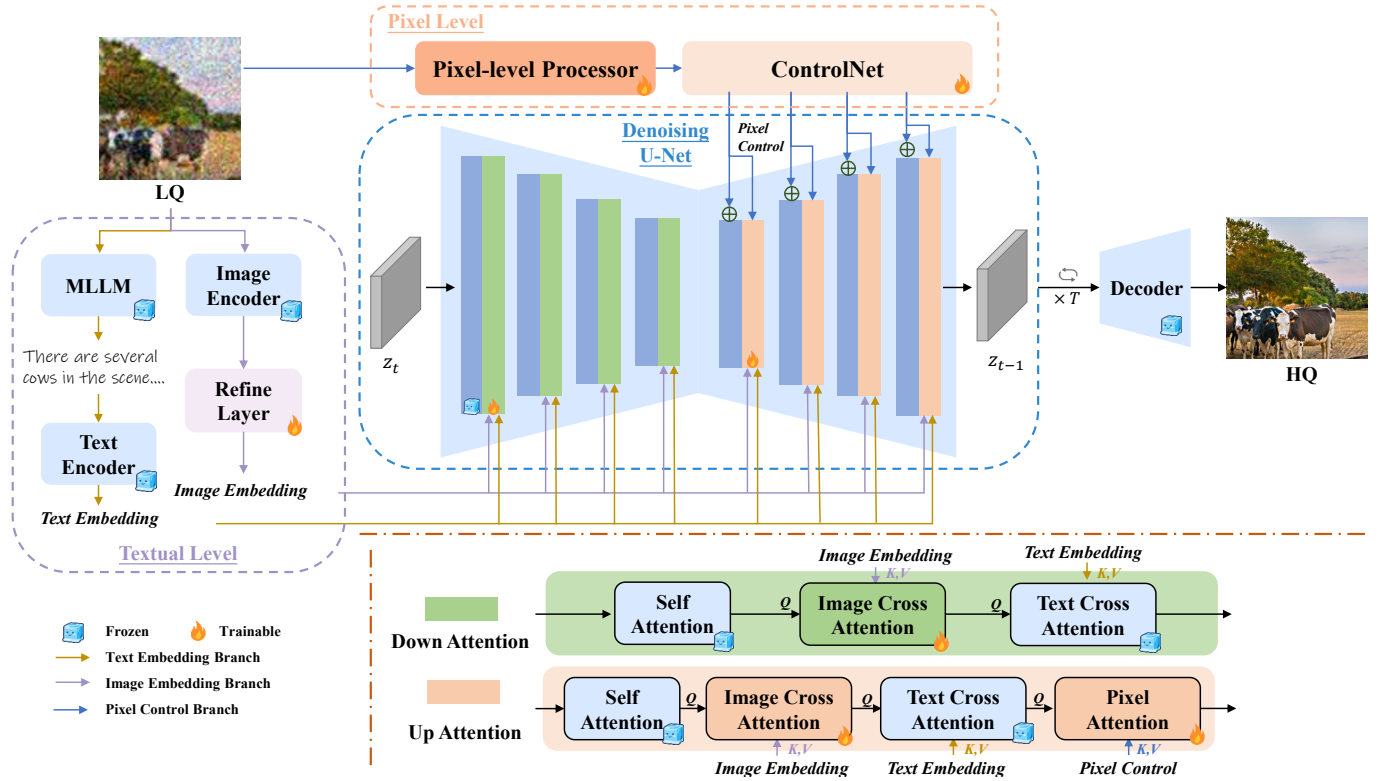


Fig. 2. The framework of the proposed method, which consists of textual level control module, pixel level control module and the denoising U-Net.

LQ images. With the aid of the powerful image understanding and reasoning capabilities of MLLM, our method can directly extract meaningful semantic information from LQ images without the need for additional training.

### B. Textual Level Restoration with MLLM

Prompt is an important factor influencing the quality and details of the generation from stable diffusion. Directly extracting prompts from low-quality images using BLIP [53] can be affected by degradation artifacts, resulting in inaccurate representations. Therefore, extracting high-quality textual representations from the original low-quality images is an important issue to consider. Previous methods, such as SeeSR and CoSeR, employed additional training to distill semantic or cognitive information from LQ images. However, these methods require extra training and their effectiveness relies on the training dataset, limiting their generalization capability.

Benefiting from multimodal large language models, which possess extensive knowledge and powerful perception and reasoning capabilities, we utilize an MLLM to predict reasonable textual representations for potential blind image restoration results. Large language models can generate promising responses to user queries based on image information. We employ the pre-trained multi-modal large language model LLaVA-7B<sup>1</sup> to predict potential clear representations from low-quality images, generating coherent high-quality textual descriptions and encoding them as text embeddings. The

forementioned process utilizes pre-trained models and does not require fine-tuning. The process can be summarized as follows:

$$T_{text} = E_{text}(E_{MLLM}(I_{LQ}, T_{input})) \quad (1)$$

where  $T_{text}$  and  $I_{LQ}$  denote the text embedding and the input low-quality image respectively,  $T_{input}$  denotes the text instruction to the MLLM, such as “Describe the image in a very detailed manner if we remove the degradation artifacts from the image.” and  $E_{text}$  and  $E_{MLLM}$  indicates the CLIP text encoder and MLLM model respectively. MLLM can take both image and text sequences as input and generate coherent descriptions as output. Compared to predicting semantic tags [31] and cognitive embeddings [32], the predicted descriptions are more detailed and conducive to human feedback.

The inference results of the MLLM include fine-grained descriptions of the restored image. To ensure that the generated image remains semantically faithful to the original low-quality image, we introduce an image embedding branch to extract visual information as a supplement. Specifically, we use CLIP image encoder to extract additional image embedding. To eliminate information about degradation artifacts present in the image embedding, we design a Refine Layer to correct the image embedding, generating image embedding that is semantically faithful to the original low-quality image but free from degradation information. The process can be expressed as follows:

$$T_{image} = E_{refine}(E_{image}(I_{LQ})) \quad (2)$$

<sup>1</sup><https://huggingface.co/liuhaotian/llava-v1.5-7b>

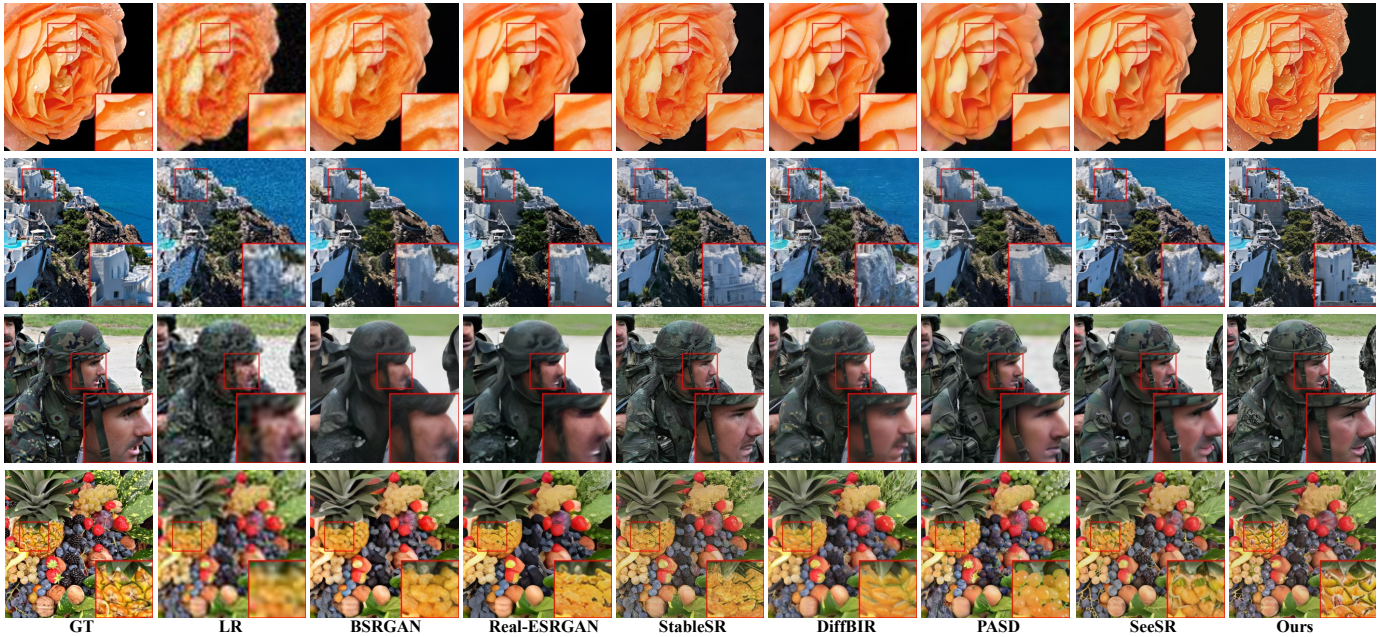


Fig. 3. Qualitative comparisons with different state-of-the-art methods on synthetic datasets. We have provided the magnified regions for clarity. **Please zoom in for a better view.**

where  $T_{image}$ ,  $E_{image}$ , and  $E_{refine}$  represent the image embedding, CLIP image encoder, and the Refine Layer respectively. The refine layer contains three MLP layers with Layer Normalization and LeakyReLU activations (except for the final layer).

Ultimately, the inferred text embedding ( $T_{text}$ ) and image embedding ( $T_{image}$ ) collaborate as the textual level information to control the restoration process of the diffusion model.

### C. Pixel Level Control with Processor

Image restoration aims to recover high-quality authentic images from low-quality images. However, real-world LQ images often suffer from complex and unknown degradation. Directly extracting features from LQ images to control the diffusion process inevitably leads to the generation of images with significant artifacts. Therefore, we propose the use of a Pixel-level Processor to mitigate the impact of degradation and obtain clear latent features from the input LQ images for controlling the diffusion process. The processor is a tiny network of four convolution layers to convert image-based conditions to  $64 \times 64$  feature space to match the diffusion process. ControlNet [52] utilizes these latent features to generate pixel control signals in the latent domain, which are used to control the denoising process of the diffusion model. The process can be formulated as follows:

$$F = E_{processor}(I_{LQ}) \quad (3)$$

$$\{P\}_{i=1}^4 = E_{ControlNet}(F) \quad (4)$$

where  $I_{LQ}$ ,  $F$ , and  $P_i$  represent the LQ image, preprocessing feature and pixel control respectively and  $E_{processor}$ ,  $E_{ControlNet}$  represent Pixel-level Processor and ControlNet module respectively.

What's more, to ensure the effectiveness of the processing operation, we use RGB loss  $L_{RGB}$  and FFT loss  $L_{FFT}$  for supervision. Specifically, we extract intermediate features with 1/2, 1/4, and 1/8 resolutions ( $F_{1/2}, F_{1/4}, F_{1/8}$ ) from the processor. Similar to PASD [30], we employ a convolutional layer to transform the feature maps at each scale into three-channel RGB space and compute the L1 distance with the corresponding high-quality images. To make further supervision and narrow gaps in the frequency domain, we make the FFT transform and calculate the loss in the frequency domain. The loss functions are computed as follows:

$$\mathcal{L}_{RGB} = \sum_{i=1/2,1/4,1/8} \|I_i - I_i^{gt}\|_1 \quad (5)$$

$$\mathcal{L}_{FFT} = \sum_{i=1/2,1/4,1/8} \|FFT(I_i) - FFT(I_i^{gt})\|_1 \quad (6)$$

where  $I_i$  denotes the RGB image transformed from  $F_i$ ,  $I_i^{gt}$  denotes the ground truth at scale  $i$  and  $FFT$  denotes the Fast Fourier transform.

### D. Integrating Control to Denoising U-Net

Based on the above textual level and pixel level components, we have obtained text embedding  $T_{text}$ , image embedding  $T_{image}$  and pixel control  $\{P_i\}_{i=1}^4$  to guide the diffusion model's denoising process. Unlike the original ControlNet, we introduce pixel attention to integrate pixel control into the denoising process. Additionally, text embedding continues to serve as textual prompts input to the original diffusion model's text cross attention, leveraging the pre-trained text-to-image generation model's prior knowledge. To enable collaboration between text embedding and image embedding, we introduce another image cross attention to integrate image embedding

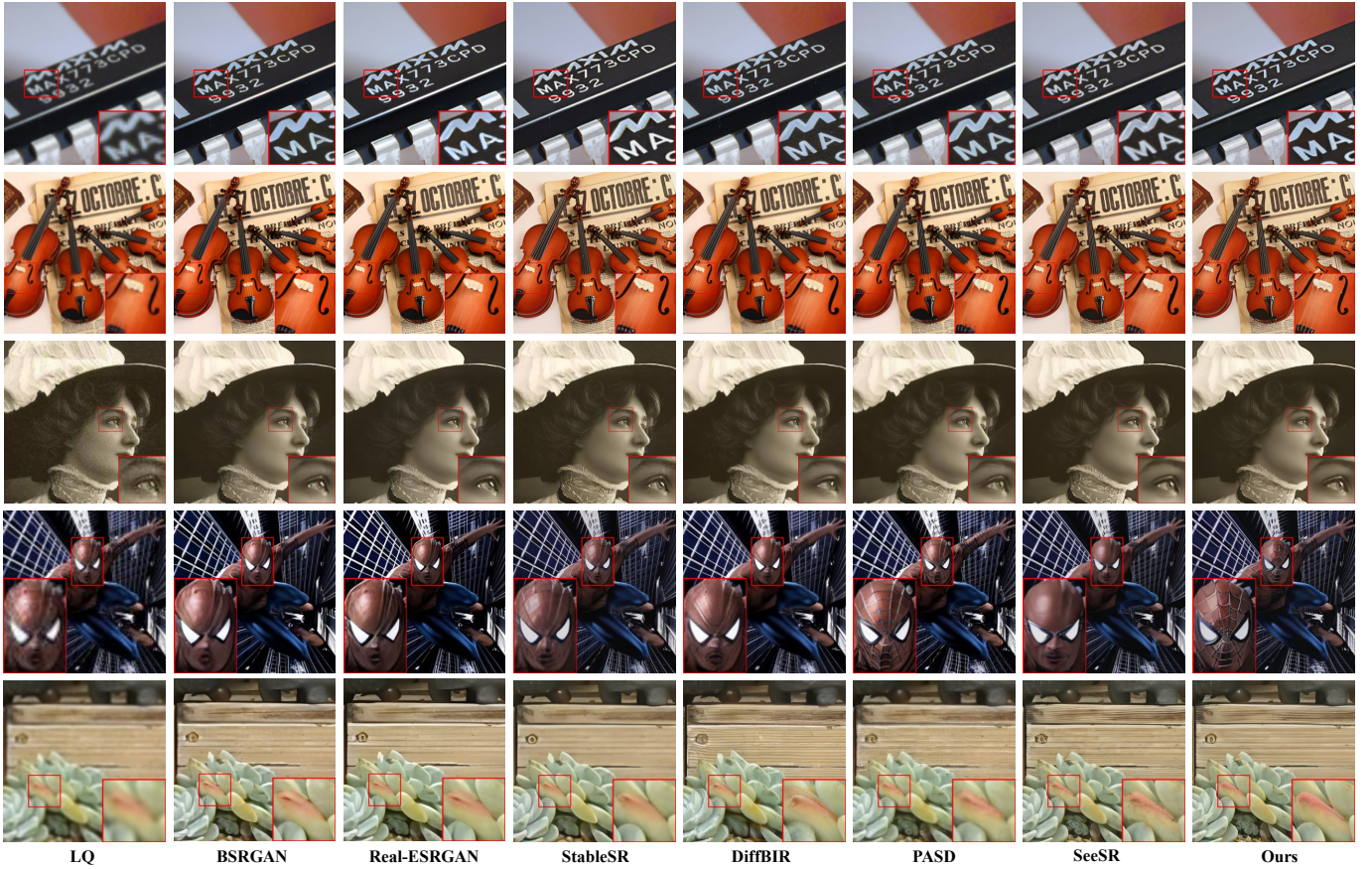


Fig. 4. Qualitative comparisons with different state-of-the-art methods on real-world datasets. We have provided the magnified regions for clarity. **Please zoom in for a better view.**

into the denoising U-Net. For the attention mechanism, we use  $Q$ ,  $K$ , and  $V$  to represent the query, key, and value features, respectively. For pixel attention,  $Q$  comes from the denoising U-Net’s features, while  $K$  and  $V$  come from the pixel control  $P_i$ . The  $K$  and  $V$  of text cross attention and image cross attention come from text embedding and image embedding, respectively. The attention module’s structure is illustrated in Fig 2, with the Down Attention and Up Attention represented in green and orange, respectively. The Down Attention module includes self-attention, image cross attention, and text cross attention. The Up Attention module includes self-attention, image cross attention, text cross attention, and pixel attention.

### E. Training and Inference Strategies

During the training process, the HQ image is encoded by the pre-trained VAE encoder [47] to obtain the latent code  $z_0$ . The diffusion process progressively adds noise to  $z_0$  to generate  $z_t$ , where  $t$  represents the random-sampled diffusion steps. By controlling the diffusion step  $t$ , the LQ image  $I_{LQ}$ , and the MLLM predicted prompt  $T_{MLLM}$ , we train the proposed image restoration network, denoted as  $\epsilon_\theta$ , to estimate the noise added to the noise layer  $z_t$ . Our optimization objective of the diffusion process is:

$$\mathcal{L}_{diff} = \mathbb{E}_{z_0, t, T_{MLLM}, I_{LQ}, \epsilon \sim \mathcal{N}} [\|\epsilon - \epsilon_\theta(z_t, t, T_{MLLM}, I_{LQ})\|_2^2] \quad (7)$$

Collaborating with (5) and (6), the final loss function is

$$\mathcal{L} = \mathcal{L}_{diff} + \lambda_1 \mathcal{L}_{RGB} + \lambda_2 \mathcal{L}_{FFT} \quad (8)$$

where  $\lambda_1$  and  $\lambda_2$  are balancing parameters. We set  $\lambda_1$  and  $\lambda_2$  equal to 0.1 and 0.01 empirically.

Specifically, the original CLIP text encoder in SD only encodes 75 tokens and cannot handle the entire generation prompts of MLLM. Therefore, we repeatedly use the text encoder to guide the encoding of all prompts. As illustrated in Fig.2, we freeze the parameters of the original SD model and only train the newly introduced modules, which include the Pixel-level Processor, ControlNet, and the newly added image attention and pixel attention within the attention module to minimize training costs.

During the inference process, we employ the classifier-free guidance strategy [54] and LRE strategy [31].

## IV. EXPERIMENTS

### A. Experimental Settings

**Implementation Details.** We employ the pre-trained SD 1.5 <sup>2</sup> model as the base pre-trained T2I model. During training, we finetune the model with Adam [55] optimizer for 100K iterations. The batch size and the learning rate are set to 32

<sup>2</sup><https://huggingface.co/runwayml/stable-diffusion-v1-5>

TABLE I  
 QUANTITATIVE COMPARISON WITH DIFFERENT STATE-OF-THE-ART METHODS ON SYNTHETIC DATASETS. THE BEST AND SECOND BEST RESULTS OF EACH METRIC ARE HIGHLIGHTED IN RED AND BLUE

Datasets	Metrics	GAN-based Methods				Diffusion-based Methods					
		BSRGAN	Real-ESRGAN	DASR	FeMaSR	LDM	StableSR	DiffBIR	PASD	SeeSR	Ours
DIV2K-Val	PSNR $\uparrow$	20.04	20.24	19.93	19.09	18.91	19.10	19.40	19.50	19.34	19.18
	SSIM $\uparrow$	0.5134	0.5352	0.5114	0.4781	0.4489	0.4414	0.4542	0.4935	0.4929	0.4918
	LPIPS $\downarrow$	0.4187	0.3913	0.4289	0.3991	0.4183	0.4121	0.4271	0.4827	0.3883	0.3840
	FID $\downarrow$	73.47	62.61	76.57	62.77	50.02	45.98	49.09	56.98	39.94	38.07
	DISTS $\downarrow$	0.2774	0.2642	0.2872	0.2459	0.2447	0.2581	0.2477	0.2725	0.2284	0.2225
	NIQE $\downarrow$	4.8133	5.0456	4.9213	4.6122	5.8359	4.7557	4.7727	5.5407	4.9767	5.0241
	MANIQA $\uparrow$	0.3513	0.3782	0.3156	0.3051	0.3481	0.3974	0.4525	0.4022	0.5134	0.5246
	MUSIQ $\uparrow$	58.78	58.48	54.22	57.74	59.31	62.60	64.59	59.15	68.70	69.27
	CLIPQA $\uparrow$	0.5200	0.5532	0.5249	0.5669	0.5997	0.6535	0.6680	0.5561	0.7062	0.7091
LSDIR-Val	PSNR $\uparrow$	16.98	16.96	16.86	16.25	16.49	16.28	16.73	16.62	16.55	16.30
	SSIM $\uparrow$	0.4122	0.4325	0.4114	0.3904	0.3826	0.3600	0.3845	0.3926	0.3965	0.3922
	LPIPS $\downarrow$	0.4533	0.4103	0.4626	0.4248	0.4403	0.4188	0.4227	0.4876	0.3976	0.3871
	FID $\downarrow$	69.00	56.59	70.74	60.41	46.11	39.58	38.72	49.72	34.79	31.85
	DISTS $\downarrow$	0.2813	0.2615	0.2892	0.2455	0.2496	0.2483	0.2318	0.2625	0.2169	0.2079
	NIQE $\downarrow$	4.1821	4.0219	4.0870	4.0970	5.6242	4.0666	4.2028	4.5963	4.3167	4.4363
	MANIQA $\uparrow$	0.3826	0.4338	0.3453	0.3333	0.3864	0.4400	0.4774	0.4269	0.5557	0.5811
	MUSIQ $\uparrow$	63.40	66.10	60.16	62.52	61.60	67.02	67.74	64.07	71.90	71.94
	CLIPQA $\uparrow$	0.5292	0.5965	0.5566	0.5848	0.5887	0.6708	0.6665	0.5692	0.7114	0.7274

and 5e-5. All experiments are conducted on an NVIDIA A100 GPU. For inference, we adopt DDPM sampling [56] with 50 timesteps.

**Training and Testing Datasets.** We train our model on DIV2K [57], Flickr2K [58], OST [59], the 9K face images from FFHQ [60] and the 20K images from LSDIR [61]. We use the degradation pipeline of Real-ESRGAN [17] to synthesize LQ-HQ training pairs. To conduct a comprehensive and reliable evaluation of the real-IR task, we conduct testing using synthetic and real-world datasets. For the synthetic test dataset, we create two datasets: DIV2K-Val and LSDIR-Val, which are generated from the DIV2K validation set [57] and the LSDIR validation set [61], respectively. For each synthetic dataset, We randomly crop 2K patches from the original validation set following the same degradation pipeline utilized during training. For the real-world test datasets, we employ the two widely used datasets, RealSR [62] and DrealSR [63] for evaluation and use the same configuration as [28] to center-crop the LQ image to  $128 \times 128$ . What’s more, We also use another real-world dataset, named RealLR200 [31], which comprises 200 LQ images that have been widely used in recent works and cover a diverse range of application scenarios.

**Evaluation Metrics.** To provide a comprehensive and effective quantitative evaluation of the different methods, we employ a range of widely used reference and non-reference metrics. In reference-based metrics, PSNR and SSIM [64] (calculated on the Y channel in YCbCr space) are fidelity metrics, while LPIPS [65] and DISTS [66] are quality evaluation metrics. FID [67] calculates the distance between the distributions of restored images and high-quality images. NIQE [68], MANIQA [69], MUSIQ [70], and CLIPQA [71] are non-reference image quality assessment (IQA) metrics. We employ the IQA-Pytorch<sup>3</sup> to compute these metrics.

**Compared Methods.** We compare our method with several state-of-the-art methods, which include GAN-based methods

(BSRGAN [16], Real-ESRGAN [17], DASR [18] and FeMaSR) and diffusion-based methods (LDM [47], StableSR [28], DiffBIR [29], PASD [30] and SeeSR [31]). We use the released version of these competing methods for testing.

## B. Experimental Results

**Qualitative Comparison.** We first provide the qualitative comparison in Fig 3 and Fig 4. For the synthetic datasets, as shown in Fig 3, GAN-based methods often produce smoother restoration results. When the image degradation is severe, they may fail to generate accurate results. In contrast, diffusion-based models can generate more detailed results. However, since StableSR and DiffBIR do not utilize semantic information to guide the diffusion model, their restoration results often lack richness in details and exhibit unclear textures. For example, the face structure (row 3) is unclear and the texture of the pineapple (row 4) is blurry. Although PASD and SeeSR take semantic information into consideration, they also produce incorrect restoration results due to inaccurate semantic predictions. As shown in Fig 3, PASD mistakenly identifies the pineapple as another fruit, resulting in an erroneous generated output (row 4) while SeeSR fails to correctly identify the building, resulting in the generation of rocks in place of the building (row 2). Additionally, benefiting from the image understanding capability of MLLM, our method is able to predict accurate semantic information from low-resolution images. Specifically, as shown in row 1, the restoration results of other methods do not include dewdrops on the flowers, while only our method’s restoration results contain dewdrops. Moreover, the structure and texture of the flowers generated by our method are more defined and clearer. To be honest, due to significant information loss in degraded images, achieving image restoration results that are comparable to ground truth is challenging and the restored images obtained through our method represent high-quality and plausible solutions.

<sup>3</sup><https://github.com/chaofengc/IQA-PyTorch>

TABLE II

QUANTITATIVE COMPARISON WITH DIFFERENT STATE-OF-THE-ART METHODS ON REAL-WORLD DATASETS. THE BEST AND SECOND BEST RESULTS OF EACH METRIC ARE HIGHLIGHTED IN RED AND BLUE. LDM IS NOT TESTED ON REALLR200 DATASET DUE TO THE LIMITATIONS OF THE RELEASED VERSION AND GPU.

Datasets	Metrics	GAN-based Methods				Diffusion-based Methods					
		BSRGAN	Real-ESRGAN	DASR	FeMaSR	LDM	StableSR	DiffBIR	PASD	SeeSR	Ours
RealSR	PSNR $\uparrow$	24.75	24.15	25.40	23.51	23.83	23.95	23.29	24.70	23.66	23.76
	SSIM $\uparrow$	0.7401	0.7363	0.7458	0.7088	0.6857	0.7240	0.6341	0.7213	0.6952	0.7088
	LPIPS $\downarrow$	0.2656	0.2710	0.3134	0.2937	0.3159	0.2604	0.3567	0.2846	0.3004	0.2865
	FID $\downarrow$	141.26	135.18	132.62	140.02	132.67	132.10	124.81	120.97	125.07	123.21
	DISTS $\downarrow$	0.2124	0.2060	0.2202	0.2286	0.2215	0.1990	0.2298	0.2040	0.2218	0.2136
	NIQE $\downarrow$	5.6362	5.8031	6.5454	5.7685	6.5139	6.6285	5.6486	5.3805	5.3968	5.5711
	MANIQA $\uparrow$	0.3764	0.3733	0.2461	0.3632	0.3635	0.3759	0.4602	0.4413	0.5369	0.5544
	MUSIQ $\uparrow$	63.29	60.37	41.20	59.06	58.91	61.81	65.29	64.48	69.70	69.81
	CLIQQA $\uparrow$	0.5116	0.4491	0.3200	0.5410	0.5680	0.5422	0.6558	0.5636	0.6680	0.6765
DrealSR	PSNR $\uparrow$	26.39	26.28	27.24	24.85	25.57	26.70	24.74	26.29	25.90	25.31
	SSIM $\uparrow$	0.7739	0.7767	0.7995	0.7247	0.7493	0.7774	0.6155	0.7475	0.7434	0.7351
	LPIPS $\downarrow$	0.2858	0.2819	0.3099	0.3157	0.3379	0.2698	0.4348	0.3320	0.3141	0.3265
	FID $\downarrow$	155.60	147.64	155.37	157.80	155.90	151.22	164.93	154.56	146.98	152.90
	DISTS $\downarrow$	0.2144	0.2089	0.2275	0.2239	0.2256	0.2066	0.2691	0.2255	0.2298	0.2347
	NIQE $\downarrow$	6.5327	6.6932	7.5868	5.9035	7.1200	7.5441	6.0035	6.7395	6.4766	6.6904
	MANIQA $\uparrow$	0.3425	0.3436	0.2845	0.3163	0.3451	0.3188	0.4553	0.4058	0.5057	0.5255
	MUSIQ $\uparrow$	57.17	54.27	42.41	53.71	53.73	51.36	61.46	56.12	64.73	66.27
	CLIQQA $\uparrow$	0.5097	0.4520	0.3815	0.5642	0.5756	0.4905	0.6574	0.5682	0.6895	0.6955
RealLR200	NIQE $\downarrow$	4.3656	4.1767	4.3180	4.6286	-	4.4676	3.7673	3.8752	4.2464	4.4406
	MANIQA $\uparrow$	0.3671	0.3633	0.2937	0.4083	-	0.3622	0.4734	0.4314	0.4845	0.5164
	MUSIQ $\uparrow$	64.87	62.96	55.71	64.24	-	61.36	67.27	66.96	68.37	67.72
	CLIQQA $\uparrow$	0.5699	0.5409	0.4689	0.6548	-	0.5545	0.7022	0.6284	0.6550	0.6930

For the real-world datasets, as shown in Fig 4, our method also generates results with reasonable structure, accurate semantics, and rich details such as the text on the chip (row 1), the string structure of the violin (row 2), the eye details (row 3), the texture details of Spider-Man’s facial details (row 4) and the structure and clarity of the succulent (row 5).

In conclusion, our method demonstrates superior performances in terms of both the rationality of structures and the clarity of details, thanks to the powerful image understanding and reasoning capabilities of MLLM, as well as the application of pixel control.

**Quantitative Comparison.** We then provide the quantitative comparison in Table I and Table II. Table I shows the quantitative results on the synthetic datasets and Table II shows the quantitative results on the real-world datasets. Compared with diffusion-based methods, our method achieves the best results in MANIQA, MUSIQ, and CLIPIQA on all five datasets, except for the score of MUSIQ on RealLR200. What’s more, our method outperforms other state-of-the-art methods in LPIPS, FID, and DISTS on the DIV2K-Val dataset and LSDIR-Val dataset. Compared with GAN-based methods, diffusion-based methods tend to get lower PSNR and SSIM scores. This is mainly because diffusion-based methods tend to generate more realistic details but at the expense of fidelity. While PSNR and SSIM are commonly used objective metrics for image quality assessment, they have limitations in capturing perceptual quality and fine details, as mentioned in [51]. Overall, our method achieves higher scores in no-reference metrics while maintaining competitive performance in full-reference measures.

**User Study.** We conduct a user study with 20 participants to assess various methods through subjective evaluation. We

compared our method with other six competitive restoration methods (BSRGAN, RealESRGAN, StableSR, DiffBIR, PASD, and SeeSR). We provided LQ images as references and asked the participants to select the best restoration result from the seven methods mentioned above. We randomly selected 26 images from synthetic and real-world datasets for testing and received evaluations from 20 participants, resulting in a total of 520 votes (26 images  $\times$  20 participants). As shown in Fig 5, our method significantly outperformed all other six competing methods, receiving 52.69% of the votes, surpassing the second-place method with 38.84% support.

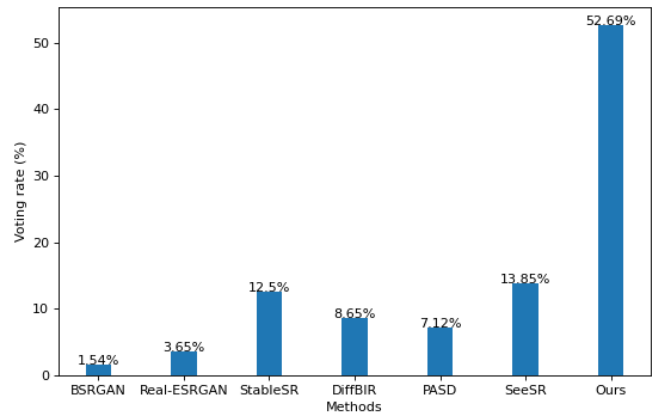


Fig. 5. User study about voting rate of 7 methods on 26 images evaluated by 20 participants.



TABLE III  
ABLATION STUDIES OF DIFFERENT PROMPTS ON DIV2K-VAL AND REALSR DATASETS.

Experiments	DIV2K-Val					RealSR				
	PSNR $\uparrow$	FID $\downarrow$	LPIPS $\downarrow$	MUSIQ $\uparrow$	CLIQQA $\uparrow$	PSNR $\uparrow$	FID $\downarrow$	LPIPS $\downarrow$	MUSIQ $\uparrow$	CLIQQA $\uparrow$
(1)	19.56	41.40	0.3806	66.20	0.6606	23.66	136.77	0.2936	68.82	0.6637
(2)	19.38	38.75	0.3864	66.11	0.6582	23.57	131.62	0.2905	68.10	0.6451
(3)	19.09	39.28	0.4001	65.77	0.6646	23.31	134.41	0.2970	69.53	0.6591
(4)	19.28	39.32	0.3903	66.35	0.6723	23.69	126.54	0.2827	66.87	0.6224
(5)	19.50	45.63	0.3973	64.90	0.6477	23.61	143.57	0.2993	69.53	0.6723
Ours	19.18	38.07	0.3840	69.27	0.7088	23.76	123.21	0.2865	69.81	0.6765

TABLE IV  
ABLATION STUDIES OF LOSS FUNCTIONS ON DIV2K-VAL AND REALSR DATASETS.

$L_{RGB}$	$L_{FFT}$	DIV2K-Val					RealSR				
		PSNR $\uparrow$	FID $\downarrow$	LPIPS $\downarrow$	MUSIQ $\uparrow$	CLIQQA $\uparrow$	PSNR $\uparrow$	FID $\downarrow$	LPIPS $\downarrow$	MUSIQ $\uparrow$	CLIQQA $\uparrow$
$\times$	$\times$	19.19	38.80	0.3954	67.03	0.6765	23.07	133.60	0.3025	68.81	0.6564
$\checkmark$	$\times$	19.16	39.24	0.3846	68.63	0.7087	23.70	125.80	0.2995	69.39	0.6644
$\times$	$\checkmark$	19.15	39.14	0.3893	68.19	0.7060	23.03	123.34	0.3028	70.21	0.6817
$\checkmark$	$\checkmark$	19.18	38.07	0.3840	69.27	0.7091	23.76	123.21	0.2865	69.81	0.6765

TABLE V  
ABLATION STUDIES OF ATTENTION MODULE ON DIV2K-VAL AND REALSR DATASETS.

Image Attention	Pixel Attention	DIV2K-Val					RealSR				
		PSNR $\uparrow$	FID $\downarrow$	LPIPS $\downarrow$	MUSIQ $\uparrow$	CLIQQA $\uparrow$	PSNR $\uparrow$	FID $\downarrow$	LPIPS $\downarrow$	MUSIQ $\uparrow$	CLIQQA $\uparrow$
$\times$	$\times$	18.87	44.41	0.4223	68.22	0.7085	22.57	139.41	0.3255	70.42	0.6740
$\checkmark$	$\times$	19.29	37.80	0.3897	65.15	0.6539	23.62	124.98	0.2787	67.26	0.6093
$\times$	$\checkmark$	19.63	45.45	0.3909	65.73	0.6416	23.81	137.25	0.2898	68.47	0.6393
$\checkmark$	$\checkmark$	19.18	38.07	0.3840	69.27	0.7091	23.76	123.21	0.2865	69.81	0.6765

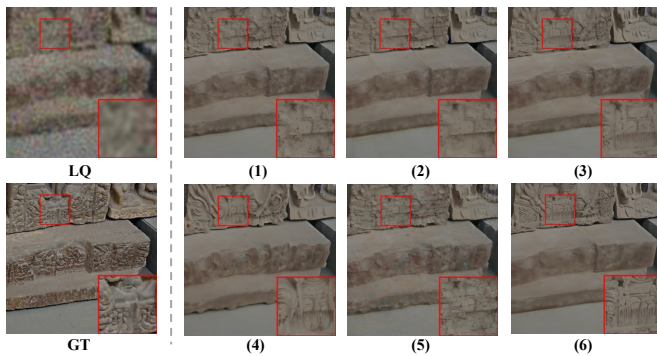


Fig. 6. Visual comparison for the ablation study of different textual level settings. (1) is the result with null prompt, (2) is the result with BLIP prompt, (3) is the result with null image embedding, (4) is the result of replacing the refine layer with only one linear layer, (5) is the result with null prompt and null image embedding, and (6) is the result of our method.

### C. Ablation Study

To validate the effectiveness of the proposed method in detail, we conducted ablation experiments from the perspectives of **textual level control**, **pixel level control**, and **attention mechanism**.

Firstly, we analyze the influence of **textual level control**, specifically the impact of text embedding and image embedding. We conduct experiments considering the following five cases:

- (1) Replacing the prompt generated by MLLM with a null prompt.
- (2) Replacing the prompt generated by MLLM with the prompt generated by BLIP.
- (3) Setting the image embedding to null.
- (4) Replacing the refine layer module with only one linear layer to project the dimension of the CLIP-encoded image embedding to the image attention dimension.
- (5) Setting both the image embedding and text embedding to null.

The results are shown in Table III and Fig 6. Table III showcases the significant enhancement in metrics such as FID, LPIPS, MUSIQ, and CLLIQQA by incorporating text embedding and image embedding. What’s more, the PSNR metric of our method remains at a comparable level. The quantitative metrics indicate that our approach excels in both semantic and texture generation, resulting in more realistic and accurate outputs. Additionally, it can be observed in Fig 6 that setting both the text embedding and image embedding to null leads to the loss of texture details. Additionally, using BLIP-generated prompts as a replacement for MLLM-generated prompts may result in suboptimal restoration outcomes due to potential inaccuracies in the prompts generated from LQ images, such as the incorrectly generated airplane in Fig 1 (b) and the engraved pattern on the stone in Fig 6 (2). Furthermore, when replacing the refine layer with only one linear layer, the lack of correction processes significantly



Fig. 7. Visual comparison for the ablation study of different loss functions settings. With the constraints of RGB loss and FFT loss, the human’s belt structure and clothing texture are more distinct.

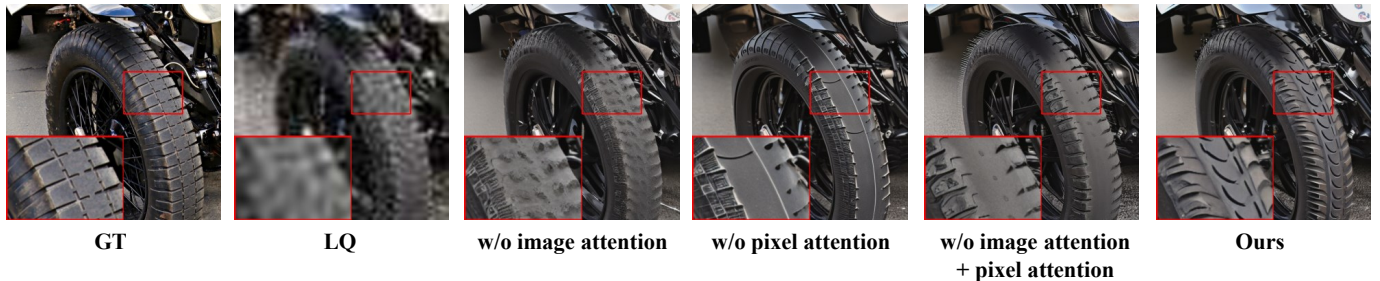


Fig. 8. Visual comparison for the ablation study of different attention settings. With the image attention and pixel attention, the tire tread pattern is more realistic and clearer.

decreases the restoration performance, specifically regarding the clarity of the statue texture highlighted by the red box in Fig 6, and leads to a decline in evaluation metrics as well.

Next, we evaluate the impact of **pixel level loss constraints** on the restoration results. The results are presented in Table IV and Fig 7. It can be observed that removing  $L_{RGB}$  and  $L_{FFT}$  leads to an overall decline in the generation quality. Although removing  $L_{RGB}$  may yield gains in terms of MUSIQ and CLIPQA metrics on the RealSR dataset, the generated details may contain artifacts and the structural details may not be sufficiently clear. As shown in Fig 7, removing  $L_{RGB}$  and  $L_{FFT}$  results in artifacts on the person’s hair, and the details of the clothing appear blurry. Removing  $L_{FFT}$  leads to an unclear structure of the belt on the person’s clothing. Removing  $L_{RGB}$  causes overall blurry artifacts on the person’s clothing. In contrast, our method performs better in terms of preserving the shape contours of the person and capturing clothing details.

Lastly, we evaluate the effectiveness of the introduced **image cross attention and pixel attention**. The experimental results are shown in Table V and Fig 8. In terms of quantitative metrics, it is evident that the removal of image attention and pixel attention leads to a significant decrease in PSNR, indicating a decline in the accuracy of the generated structural details. Simultaneously, the individual removal of image attention and pixel attention impacts metrics such as FID and MUSIQ, which assess the quality of the generated images. Our method achieves a trade-off between realism and fidelity. Visually, it can be observed in Fig 8 that when removing image attention, the texture of the tire is not very clear. When removing pixel attention, although the texture of the tire is clear, the structural details of the tire’s texture are incomplete.

When removing image attention and pixel attention, both the texture structure and clarity are compromised. Our method achieves better results in terms of structure and clarity thanks to both image attention and pixel attention being employed.

## V. CONCLUSION

In this paper, we propose a novel multimodal-perception approach for realistic image restoration based on the diffusion model. We consider both textual level and pixel level perspectives to solve the restoration problem. Regarding textual level information, we utilize the multimodal large language model to infer reliable semantic text representations from low-quality images. Additionally, we design the Refine Layer to generate the corrected image embeddings, which collaborate with MLLM to achieve a balance between fidelity and realism. For structural control in generating images, we employ the Pixel-level Processor and ControlNet for pixel control. Lastly, we integrate the control information and the diffusion model using the attention mechanism, enabling high-fidelity and high-realism image restoration. Our method demonstrates state-of-the-art performance on multiple datasets both qualitatively and quantitatively.

To be honest, due to the utilization of the MLLM and diffusion model, our approach requires higher computational resources and longer inference time. However, We hope that this work serves as an inspiration for the application of MLLM in diffusion-based image restoration and provides valuable insights for future research endeavors. We acknowledge the need to explore more efficient and concise methods for image restoration and researching more efficient and concise methods for image restoration is also a direction we will pursue in the future.

## REFERENCES

- [1] C. Dong, C. C. Loy, and X. Tang, "Accelerating the super-resolution convolutional neural network," in *Computer Vision—ECCV 2016: 14th European Conference, Amsterdam, The Netherlands, October 11–14, 2016, Proceedings, Part II 14*. Springer, 2016, pp. 391–407.
- [2] H. Zhao, X. Kong, J. He, Y. Qiao, and C. Dong, "Efficient image super-resolution using pixel attention," in *Computer Vision—ECCV 2020 Workshops: Glasgow, UK, August 23–28, 2020, Proceedings, Part III 16*. Springer, 2020, pp. 56–72.
- [3] Z. Chen, Y. Zhang, J. Gu, L. Kong, X. Yang, and F. Yu, "Dual aggregation transformer for image super-resolution," in *Proceedings of the IEEE/CVF international conference on computer vision*, 2023, pp. 12 312–12 321.
- [4] O. Kupyn, V. Budzan, M. Mykhailych, D. Mishkin, and J. Matas, "Deblurgan: Blind motion deblurring using conditional adversarial networks," in *Proceedings of the IEEE conference on computer vision and pattern recognition*, 2018, pp. 8183–8192.
- [5] O. Kupyn, T. Martyniuk, J. Wu, and Z. Wang, "Deblurgan-v2: Deblurring (orders-of-magnitude) faster and better," in *Proceedings of the IEEE/CVF international conference on computer vision*, 2019, pp. 8878–8887.
- [6] Z. Chen, Y. Zhang, D. Liu, J. Gu, L. Kong, X. Yuan *et al.*, "Hierarchical integration diffusion model for realistic image deblurring," *Advances in Neural Information Processing Systems*, vol. 36, 2024.
- [7] K. Zhang, W. Zuo, Y. Chen, D. Meng, and L. Zhang, "Beyond a gaussian denoiser: Residual learning of deep cnn for image denoising," *IEEE transactions on image processing*, vol. 26, no. 7, pp. 3142–3155, 2017.
- [8] K. Zhang, W. Zuo, and L. Zhang, "Ffdnet: Toward a fast and flexible solution for cnn-based image denoising," *IEEE Transactions on Image Processing*, vol. 27, no. 9, pp. 4608–4622, 2018.
- [9] H. Zeng, J. Cai, L. Li, Z. Cao, and L. Zhang, "Learning image-adaptive 3d lookup tables for high performance photo enhancement in real-time," *IEEE Transactions on Pattern Analysis and Machine Intelligence*, vol. 44, no. 4, pp. 2058–2073, 2020.
- [10] Y. Zhang, H. Zhang, L. Song, R. Xie, and W. Zhang, "Dual-head fusion network for image enhancement," in *ICASSP 2023-2023 IEEE International Conference on Acoustics, Speech and Signal Processing (ICASSP)*. IEEE, 2023, pp. 1–5.
- [11] R. Suvorov, E. Logacheva, A. Mashikhin, A. Remizova, A. Ashukha, A. Silvestrov, N. Kong, H. Goka, K. Park, and V. Lempitsky, "Resolution-robust large mask inpainting with fourier convolutions," in *Proceedings of the IEEE/CVF winter conference on applications of computer vision*, 2022, pp. 2149–2159.
- [12] A. Lugmayr, M. Danelljan, A. Romero, F. Yu, R. Timofte, and L. Van Gool, "Repaint: Inpainting using denoising diffusion probabilistic models," in *Proceedings of the IEEE/CVF conference on computer vision and pattern recognition*, 2022, pp. 11 461–11 471.
- [13] C. Corneanu, R. Gadede, and A. M. Martinez, "Latentpaint: Image inpainting in latent space with diffusion models," in *Proceedings of the IEEE/CVF Winter Conference on Applications of Computer Vision*, 2024, pp. 4334–4343.
- [14] X. Fu, X. Wang, A. Liu, J. Han, and Z.-J. Zha, "Learning dual priors for jpeg compression artifacts removal," in *Proceedings of the IEEE/CVF international conference on computer vision*, 2021, pp. 4086–4095.
- [15] B. Kwar, J. Song, S. Ermon, and M. Elad, "Jpeg artifact correction using denoising diffusion restoration models," *arXiv preprint arXiv:2209.11888*, 2022.
- [16] K. Zhang, J. Liang, L. Van Gool, and R. Timofte, "Designing a practical degradation model for deep blind image super-resolution," in *Proceedings of the IEEE/CVF International Conference on Computer Vision*, 2021, pp. 4791–4800.
- [17] X. Wang, L. Xie, C. Dong, and Y. Shan, "Real-esrgan: Training real-world blind super-resolution with pure synthetic data," in *Proceedings of the IEEE/CVF international conference on computer vision*, 2021, pp. 1905–1914.
- [18] J. Liang, H. Zeng, and L. Zhang, "Efficient and degradation-adaptive network for real-world image super-resolution," in *European Conference on Computer Vision*. Springer, 2022, pp. 574–591.
- [19] C. Chen, X. Shi, Y. Qin, X. Li, X. Han, T. Yang, and S. Guo, "Real-world blind super-resolution via feature matching with implicit high-resolution priors," in *Proceedings of the 30th ACM International Conference on Multimedia*, 2022, pp. 1329–1338.
- [20] J. Liang, H. Zeng, and L. Zhang, "Details or artifacts: A locally discriminative learning approach to realistic image super-resolution," in *Proceedings of the IEEE/CVF Conference on Computer Vision and Pattern Recognition*, 2022, pp. 5657–5666.
- [21] L. Xie, X. Wang, X. Chen, G. Li, Y. Shan, J. Zhou, and C. Dong, "Desra: detect and delete the artifacts of gan-based real-world super-resolution models," *arXiv preprint arXiv:2307.02457*, 2023.
- [22] J. Ho, A. Jain, and P. Abbeel, "Denoising diffusion probabilistic models," *Advances in neural information processing systems*, vol. 33, pp. 6840–6851, 2020.
- [23] P. Dhariwal and A. Nichol, "Diffusion models beat gans on image synthesis," *Advances in neural information processing systems*, vol. 34, pp. 8780–8794, 2021.
- [24] B. Kwar, M. Elad, S. Ermon, and J. Song, "Denoising diffusion restoration models," *Advances in Neural Information Processing Systems*, vol. 35, pp. 23 593–23 606, 2022.
- [25] Y. Wang, J. Yu, and J. Zhang, "Zero-shot image restoration using denoising diffusion null-space model," *arXiv preprint arXiv:2212.00490*, 2022.
- [26] C. Saharia, J. Ho, W. Chan, T. Salimans, D. J. Fleet, and M. Norouzi, "Image super-resolution via iterative refinement," *IEEE transactions on pattern analysis and machine intelligence*, vol. 45, no. 4, pp. 4713–4726, 2022.
- [27] B. Fei, Z. Lyu, L. Pan, J. Zhang, W. Yang, T. Luo, B. Zhang, and B. Dai, "Generative diffusion prior for unified image restoration and enhancement," in *Proceedings of the IEEE/CVF Conference on Computer Vision and Pattern Recognition*, 2023, pp. 9935–9946.
- [28] J. Wang, Z. Yue, S. Zhou, K. C. Chan, and C. C. Loy, "Exploiting diffusion prior for real-world image super-resolution," *arXiv preprint arXiv:2305.07015*, 2023.
- [29] X. Lin, J. He, Z. Chen, Z. Lyu, B. Fei, B. Dai, W. Ouyang, Y. Qiao, and C. Dong, "Diffbir: Towards blind image restoration with generative diffusion prior," *arXiv preprint arXiv:2308.15070*, 2023.
- [30] T. Yang, P. Ren, X. Xie, and L. Zhang, "Pixel-aware stable diffusion for realistic image super-resolution and personalized stylization," *arXiv preprint arXiv:2308.14469*, 2023.
- [31] R. Wu, T. Yang, L. Sun, Z. Zhang, S. Li, and L. Zhang, "Seesr: Towards semantics-aware real-world image super-resolution," *arXiv preprint arXiv:2311.16518*, 2023.
- [32] H. Sun, W. Li, J. Liu, H. Chen, R. Pei, X. Zou, Y. Yan, and Y. Yang, "Coser: Bridging image and language for cognitive super-resolution," *arXiv preprint arXiv:2311.16512*, 2023.
- [33] J. Y. Koh, D. Fried, and R. R. Salakhutdinov, "Generating images with multimodal language models," *Advances in Neural Information Processing Systems*, vol. 36, 2024.
- [34] X. Jin, Y. Shi, B. Xia, and W. Yang, "Llmra: Multi-modal large language model based restoration assistant," *arXiv preprint arXiv:2401.11401*, 2024.
- [35] T.-J. Fu, W. Hu, X. Du, W. Y. Wang, Y. Yang, and Z. Gan, "Guiding instruction-based image editing via multimodal large language models," *arXiv preprint arXiv:2309.17102*, 2023.
- [36] Y. Huang, L. Xie, X. Wang, Z. Yuan, X. Cun, Y. Ge, J. Zhou, C. Dong, R. Huang, R. Zhang *et al.*, "Smartedit: Exploring complex instruction-based image editing with multimodal large language models," *arXiv preprint arXiv:2312.06739*, 2023.
- [37] F. Mu, L. Shi, S. Wang, Z. Yu, B. Zhang, C. Wang, S. Liu, and Q. Wang, "Clarifygpt: Empowering llm-based code generation with intention clarification," *arXiv preprint arXiv:2310.10996*, 2023.
- [38] W. Guan, H. Li, D. Xu, J. Liu, S. Gong, and J. Liu, "Frequency generation for real-world image super-resolution," *IEEE Transactions on Circuits and Systems for Video Technology*, 2024.
- [39] Y. Qiu, Q. Zhu, S. Zhu, and B. Zeng, "Dual circle contrastive learning-based blind image super-resolution," *IEEE Transactions on Circuits and Systems for Video Technology*, 2023.
- [40] G.-Y. Chen, W.-D. Weng, J.-N. Su, M. Gan, and C. P. Chen, "Dynamic degradation intensity estimation for adaptive blind super-resolution: A novel approach and benchmark dataset," *IEEE Transactions on Circuits and Systems for Video Technology*, 2023.
- [41] S. Ding, Q. Wang, L. Guo, X. Li, L. Ding, and X. Wu, "Wavelet and adaptive coordinate attention guided fine-grained residual network for image denoising," *IEEE Transactions on Circuits and Systems for Video Technology*, 2024.
- [42] J. Liang, J. Cao, G. Sun, K. Zhang, L. Van Gool, and R. Timofte, "Swinir: Image restoration using swin transformer," in *Proceedings of the IEEE/CVF international conference on computer vision*, 2021, pp. 1833–1844.
- [43] L. Chen, X. Chu, X. Zhang, and J. Sun, "Simple baselines for image restoration," in *European conference on computer vision*. Springer, 2022, pp. 17–33.

- [44] S. W. Zamir, A. Arora, S. Khan, M. Hayat, F. S. Khan, and M.-H. Yang, “Restormer: Efficient transformer for high-resolution image restoration,” in *Proceedings of the IEEE/CVF conference on computer vision and pattern recognition*, 2022, pp. 5728–5739.
- [45] J. Dong, H. Bai, J. Tang, and J. Pan, “Deep unpaired blind image super-resolution using self-supervised learning and exemplar distillation,” *International Journal of Computer Vision*, pp. 1–14, 2023.
- [46] J. Song, C. Meng, and S. Ermon, “Denoising diffusion implicit models,” *arXiv preprint arXiv:2010.02502*, 2020.
- [47] R. Rombach, A. Blattmann, D. Lorenz, P. Esser, and B. Ommer, “High-resolution image synthesis with latent diffusion models,” in *Proceedings of the IEEE/CVF conference on computer vision and pattern recognition*, 2022, pp. 10 684–10 695.
- [48] S. Zhou, K. Chan, C. Li, and C. C. Loy, “Towards robust blind face restoration with codebook lookup transformer,” *Advances in Neural Information Processing Systems*, vol. 35, pp. 30 599–30 611, 2022.
- [49] Y. Zhang, X. Huang, J. Ma, Z. Li, Z. Luo, Y. Xie, Y. Qin, T. Luo, Y. Li, S. Liu *et al.*, “Recognize anything: A strong image tagging model,” *arXiv preprint arXiv:2306.03514*, 2023.
- [50] J. Wu, X. Li, C. Si, S. Zhou, J. Yang, J. Zhang, Y. Li, K. Chen, Y. Tong, Z. Liu *et al.*, “Towards language-driven video inpainting via multimodal large language models,” *arXiv preprint arXiv:2401.10226*, 2024.
- [51] F. Yu, J. Gu, Z. Li, J. Hu, X. Kong, X. Wang, J. He, Y. Qiao, and C. Dong, “Scaling up to excellence: Practicing model scaling for photo-realistic image restoration in the wild,” *arXiv preprint arXiv:2401.13627*, 2024.
- [52] L. Zhang, A. Rao, and M. Agrawala, “Adding conditional control to text-to-image diffusion models,” in *Proceedings of the IEEE/CVF International Conference on Computer Vision*, 2023, pp. 3836–3847.
- [53] J. Li, D. Li, C. Xiong, and S. Hoi, “Blip: Bootstrapping language-image pre-training for unified vision-language understanding and generation,” in *International conference on machine learning*. PMLR, 2022, pp. 12 888–12 900.
- [54] J. Ho and T. Salimans, “Classifier-free diffusion guidance,” *arXiv preprint arXiv:2207.12598*, 2022.
- [55] D. P. Kingma and J. Ba, “Adam: A method for stochastic optimization,” *arXiv preprint arXiv:1412.6980*, 2014.
- [56] A. Q. Nichol and P. Dhariwal, “Improved denoising diffusion probabilistic models,” in *International conference on machine learning*. PMLR, 2021, pp. 8162–8171.
- [57] E. Agustsson and R. Timofte, “Ntire 2017 challenge on single image super-resolution: Dataset and study,” in *Proceedings of the IEEE conference on computer vision and pattern recognition workshops*, 2017, pp. 126–135.
- [58] R. Timofte, E. Agustsson, L. Van Gool, M.-H. Yang, and L. Zhang, “Ntire 2017 challenge on single image super-resolution: Methods and results,” in *Proceedings of the IEEE conference on computer vision and pattern recognition workshops*, 2017, pp. 114–125.
- [59] X. Wang, K. Yu, C. Dong, and C. C. Loy, “Recovering realistic texture in image super-resolution by deep spatial feature transform,” in *Proceedings of the IEEE conference on computer vision and pattern recognition*, 2018, pp. 606–615.
- [60] T. Karras, S. Laine, and T. Aila, “A style-based generator architecture for generative adversarial networks,” in *Proceedings of the IEEE/CVF conference on computer vision and pattern recognition*, 2019, pp. 4401–4410.
- [61] Y. Li, K. Zhang, J. Liang, J. Cao, C. Liu, R. Gong, Y. Zhang, H. Tang, Y. Liu, D. Demandolx *et al.*, “Lsdir: A large scale dataset for image restoration,” in *Proceedings of the IEEE/CVF Conference on Computer Vision and Pattern Recognition*, 2023, pp. 1775–1787.
- [62] J. Cai, H. Zeng, H. Yong, Z. Cao, and L. Zhang, “Toward real-world single image super-resolution: A new benchmark and a new model,” in *Proceedings of the IEEE/CVF international conference on computer vision*, 2019, pp. 3086–3095.
- [63] P. Wei, Z. Xie, H. Lu, Z. Zhan, Q. Ye, W. Zuo, and L. Lin, “Component divide-and-conquer for real-world image super-resolution,” in *Computer Vision—ECCV 2020: 16th European Conference, Glasgow, UK, August 23–28, 2020, Proceedings, Part VIII 16*. Springer, 2020, pp. 101–117.
- [64] Z. Wang, A. C. Bovik, H. R. Sheikh, and E. P. Simoncelli, “Image quality assessment: from error visibility to structural similarity,” *IEEE transactions on image processing*, vol. 13, no. 4, pp. 600–612, 2004.
- [65] R. Zhang, P. Isola, A. A. Efros, E. Shechtman, and O. Wang, “The unreasonable effectiveness of deep features as a perceptual metric,” in *Proceedings of the IEEE conference on computer vision and pattern recognition*, 2018, pp. 586–595.
- [66] K. Ding, K. Ma, S. Wang, and E. P. Simoncelli, “Image quality assessment: Unifying structure and texture similarity,” *IEEE transactions on pattern analysis and machine intelligence*, vol. 44, no. 5, pp. 2567–2581, 2020.
- [67] M. Heusel, H. Ramsauer, T. Unterthiner, B. Nessler, and S. Hochreiter, “Gans trained by a two time-scale update rule converge to a local nash equilibrium,” *Advances in neural information processing systems*, vol. 30, 2017.
- [68] L. Zhang, L. Zhang, and A. C. Bovik, “A feature-enriched completely blind image quality evaluator,” *IEEE Transactions on Image Processing*, vol. 24, no. 8, pp. 2579–2591, 2015.
- [69] S. Yang, T. Wu, S. Shi, S. Lao, Y. Gong, M. Cao, J. Wang, and Y. Yang, “Maniqa: Multi-dimension attention network for no-reference image quality assessment,” in *Proceedings of the IEEE/CVF Conference on Computer Vision and Pattern Recognition*, 2022, pp. 1191–1200.
- [70] J. Ke, Q. Wang, Y. Wang, P. Milanfar, and F. Yang, “Musiq: Multi-scale image quality transformer,” in *Proceedings of the IEEE/CVF international conference on computer vision*, 2021, pp. 5148–5157.
- [71] J. Wang, K. C. Chan, and C. C. Loy, “Exploring clip for assessing the look and feel of images,” in *Proceedings of the AAAI Conference on Artificial Intelligence*, vol. 37, no. 2, 2023, pp. 2555–2563.